Impurity seeding for tokamak power exhaust: from present devices via ITER to DEMO

A. Kallenbach[1], M. Bernert[1], R. Dux[1], L. Casali[1], T. Eich[1], L. Giannone[1], A. Herrmann[1], R. McDermott[1], A. Mlynek[1], H.W. Müller[1], F. Reimold[1], J. Schweinzer[1], M. Sertoli[1], G. Tardini[1], W. Treutterer[1], E. Viezzer[1], R. Wenninger[*], M. Wischmeier[1], ASDEX Upgrade Team

[1]Max Planck Institute for Plasma Physics, EURATOM Association, D-85748 Garching, Germany
[*]EFDA PPP&T department, D-85748 Garching, Germany

Abstract. A future fusion reactor is expected to have all-metal plasma facing materials (PFM) to ensure low erosion rates, low tritium retention and stability against high neutron fluences. As a consequence, intrinsic radiation losses in the plasma edge and divertor are low in comparison to devices with carbon PFMs. To avoid localized overheating in the divertor, intrinsic low-Z and medium-Z impurities have to be inserted into the plasma to convert a major part of the power flux into radiation and to facilitate partial divertor detachment. For burning plasma conditions in ITER, which operates not far above the L-H threshold power, a high divertor radiation level will be mandatory to avoid thermal overload of divertor components. Moreover, in a prototype reactor, DEMO, a high main plasma radiation level will be required in addition for dissipation of the much higher alpha heating power. For divertor plasma conditions in present day tokamaks and in ITER, nitrogen appears most suitable regarding its radiative characteristics. If elevated main chamber radiation is desired as well, argon is the best candidate for simulataneous enhancement of core and divertor radiation, provided sufficient divertor compression can be obtained. The parameter P_{sep}/R, the power flux through the separatrix normalized by the major radius, is suggested as a suitable scaling (for a given electron density) for the extrapolation of present day divertor conditions to larger devices. The scaling for main chamber radiation from small to large devices has a higher, more favourable dependence of about $P_{rad,main}/R^2$. Krypton provides the smallest fuel dilution for DEMO conditions, but has a more centrally peaked radiation profile compared to argon. For investigation of the different effects of main chamber and divertor radiation and for optimization of their distribution, a double radiative feedback system has been implemented in ASDEX Upgrade. About half the ITER/DEMO values of P_{sep}/R have been achieved so far, and close to DEMO values of $P_{rad,main}/R^2$, albeit at lower P_{sep}/R. Further increase of this parameter may be achieved by increase of the neutral pressure or improved divertor geometry.

1. Introduction

For a burning plasma device like ITER, radiative power removal by seed impurities will be inevitable to avoid divertor damage by excessive heat flux [1] [2] and to limit target plate erosion to acceptable values [3]. In ITER, divertor impurity seed radiation has to be used for power dissipation and promotion of partial detachment of the outer divertor. This leads to a drastic reduction of the heat flux at the separatrix and a few cm upward along the target. The inner divertor shows generally more pronounced detachment compared to the outer divertor and is thus regarded noncritical. Owing to the high power influx, the ITER divertor operation will be close to the technical and physical limits. However, due to the proximity of the ITER heating power (150 MW for Q=10) to the L-H threshold power ($\approx$ 70 MW), strong core radiation will not be permitted. In a future DEMO prototype reactor, much higher heating powers ($\approx$ 500 MW) are expected compared to ITER. Considerable main chamber radiation ($\approx$ 350 MW) will be required to avoid divertor heat overload. Given a standard vertical target divertor as a reference design, the DEMO divertor performance will be comparable to ITER and allowed peak heat flux values of 5-10 MW/m^2 are expected. Conceptual improvements of the DEMO divertor will compensate negative effects of high neutron loads on plasma facing materials and structural components at first [4]. Recent investigations [5] [6] on the scaling of the heat flux width predict smaller, i.e. more challenging values for ITER and DEMO. On the positive side, the lack of a size dependence of the power width λ_q enables divertor identity experiments in present day devices, with unmitigated (fully attached) power widths, as measured along the target plate, of the order $\lambda_{int,tar}$= 15 - 20 mm in ITER, DEMO and ASDEX Upgrade (AUG) [7]. For identical upstream separatrix electron density (n$_{e,sep,omp}$ $\approx$ 5 10^{19} m^{-3}) and divertor neutral pressure ($\approx$ 10 Pa) [8], the ratio of power flux through the separatrix and major radius, P$_{sep}$/R, is assumed as the divertor identity parameter [9]. The divertor radiation scales linearly with major radius under these conditions. ITER- or DEMO-like values of P$_{sep}$/R have not been achieved in an existing tokamak so far. AUG is pursuing this target and has demonstrated half of the required value of P$_{sep}$/R= 15 MW/m, with perspectives for further increase and no critical limits hit so far [10]. Seeding scenarios must achieve sufficient energy confinement simultaneous with a high radiation level. In fact, the effect of impurity seeding on energy confinement shows a very rich phenomenology [11] [12] [13] [14]. The most recent results are described in [15].

This paper reviews the basic processes and current achievements of impurity seeding concentrating on AUG high power discharges. It is organized as follows. Section 2 introduces atomic data and radiative loss functions for possible seed impurity species. To avoid unacceptable tritium co-deposition, only recycling impurities are considered . Analytical estimates of core and divertor radiation are introduced in section 3. Radiation cooling experiments in AUG are described in section 4. The effect of tungsten sputtering by the seed impurities is addressed in section 5. Finally, in section 6 predictions for radiative cooling in DEMO are given and some conclusions are drawn in section 7.
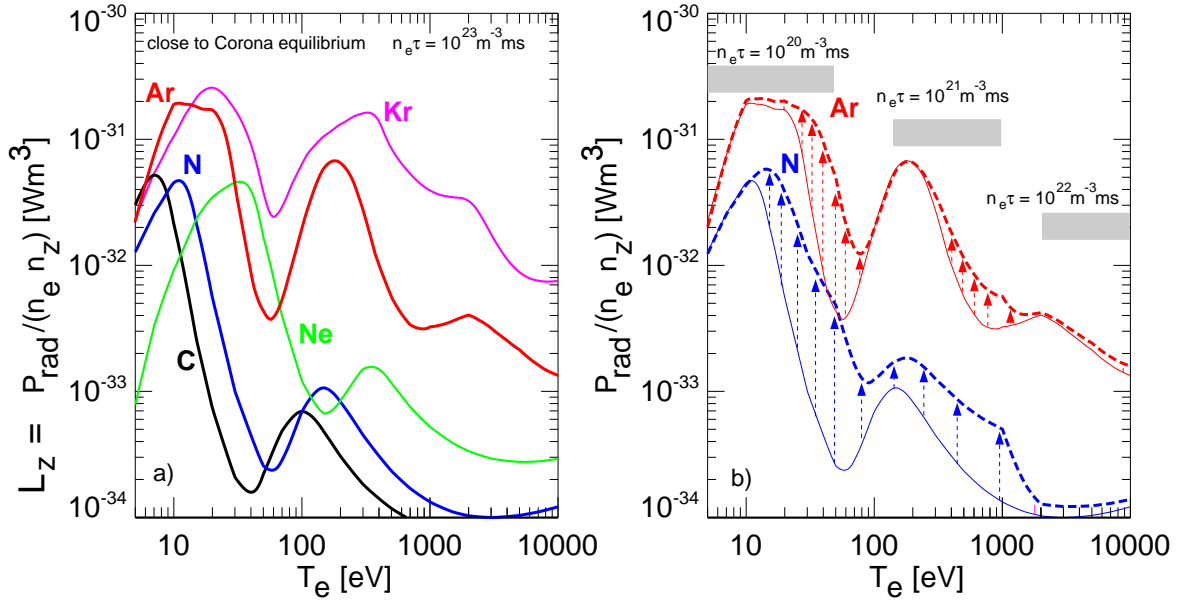
Figure 1. *Radiative loss parameter L_z for seed impurities from ADAS and an electron density of 10^{20} m^{-3}, as the sum of line radiation, recombination-induced radiation and bremsstrahlung. a) Data for carbon, nitrogen, neon, argon and krypton in coronal equilibrium. b) non-equilibrium enhanced values for N and Ar (dashed lines). Appropriate values for the non-equilibrium parameter $n_e\tau$ are used for the divertor and pedestal parameter regions as indicated by the broad horizontal bars. In between the T_e values marked, a linear interpolation of $n_e\tau$ in T_e was used to obtain smooth curves.*

2. Atomic data

The radiative loss power for an impurity species can be calculated from rate coefficients for ionization, recombination and line excitation using a collisonal-radiative model. Figure 1 shows the total loss power L_z for a number of impurities from ADAS [16]. The loss power is the sum of the emission of individual spectral lines and continuum emission. Since not all possible transitions are considered, in particular between high lying states, the L_z values shown may moderately underestimate the true losses. For core plasma conditions, where ionisation and recombination times are much shorter than the impurity residence time, the coronal equilibrium approximation is appropriate (figure 1a). This does not hold for the divertor, where the impurity residence time may be less than a millisecond and, to a lesser extent, to the pedestal where ELMs lead to frequent re-organization of profiles and influxes. Non-quilibrium conditions mostly lead to an enhancement of the radiative power during the ionization to the equilibrium charge state. Details of the underlying effects can be found in [17]. The situation is illustrated in figure 2. A neutral N atom is inserted into a plasma and the evolution of charge state and radiated power are calculated using collisional-radiative modelling. While being ionised, radiation is emitted which decreases in time while

the equilibrium ionisation state is approached. Here, the early radiation in the low ionized states is responsible for the non-equilibrium enhancement. L_z is calculated
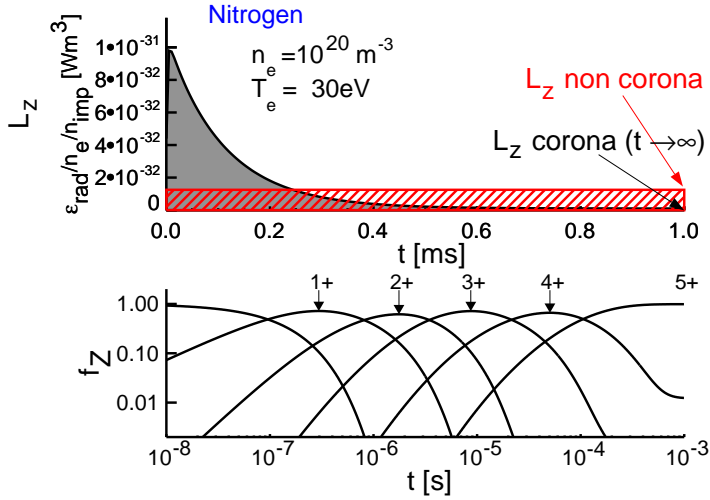

Figure 2. *Origin of non-equilibrium effects on L_z for the situation of a neutral nitrogen atom put into a 30 eV plasma for the duration τ. During ionization to its equilbrium state, radiation losses are enhanced. The non-equilibrium L_z value is the average radiated power over the time τ, which can be identified with a characteristic residence time. The energy radiated by an atom during the time τ is called radiative potential [18], its value is 7.8 keV for the present conditions.*

using the time-averaged radiation during the residence time τ. For long times τ, the non-equilibrium L_z values approach the coronal equilibrium values. Figure 1b shows corresponding values of L_z for nitrogen and argon using a simple estimate for the non-equilibrium parameter $n_e\tau$. Here, n_e is the measure for the inverse collisional time scale. The radiation enhancement is more pronounced for the lower-Z atom N compared to Ar. Non-equilibrium effects also increase the radiative losses in the pedestal region. Plasma parameter variations caused by ELMs lead here to additional deviations from coronal equilibrium. For a realistic calculation of impurity radiation in the pedestal and SOL regions, ELMs have to be incorporated in a self-consistent way. For larger devices the impact of non-equilibrium effects in the core plasma is expected to decrease due to longer time scales τ in comparison to smaller devices. Comparing the atomic data of the species considered, argon exhibits the highest radiative efficiency for the temperature range of the divertor. However, its high radiative losses in the core plasma do not permit high Ar concentrations unless a very high compression in the divertor can be obtained. Such a compression has been obtained in DIII-D 'puff and pump' experiments where the strike point was positioned at the throat of the pumping line [19], but this is not easily achieved with a standard closed divertor configuration where the pump is attached to a volume filled with nearly wall-thermalized D molecules. Neon exhibits a relatively small radiative loss power at low temperatures. Indeed, JET reports a reduction of divertor radiation with Ne seeding [14] due to more core localised radiation.

4

3. Analytical description of radiation losses

3.1. Core radiation

The prediction of core radiated power based on atomic data requires the knowledge of the electron density, the electron temperature and the impurity concentration c_z. The local radiated power density is obtained by the product $L_z\, n_e^2\, c_z$. The impurity concentration needs to be measured or calculated from theory. We assume flat impurity concentration profiles in the following, $c_z(\rho)=$ const. A complication enters via the non-equilibrium enhancement of radiation losses, which is expected to be important in the pedestal region. In figure 1b, the enhancement is described by a corresponding non-equilibrium parameter $n_e(\rho)\, \tau_p(\rho)$ as used in the divertor region. This assumes a neutral impurity source which results in a less accurate radiation prediction in the pedestal compared to divertor conditions. A dedicated impurity transport calculation for the determination of non-equilibrium radiation enhancement in the pedestal region has been done with the STRAHL code, simulating 100 Hz ELMs [20]. Indeed, comparsion of the ELM-cycle averaged radiation showed substantial enhancements of more than an order of magnitude, compared to corona equilibrium values closely outside the separatrix. However, a reduction of radiation due to non-equilibrium conditions is present in a narrow range just inside the separatrix. As in the simple model of figure 1, the enhancement is largest for small Z impurities. The STRAHL model clearly showed that a realistic ELM model and time-dependent calculations are required to predict accurate H-mode radiation profiles in the pedestal region, but a 2-D code is required to address the effects of poloidal asymmetries and drifts. Predicted core radiation profiles for coronal and non-equilibrium conditions with the simple model are shown in section 4 for ASDEX Upgrade and DEMO-like conditions.

3.2. Divertor radiation

The calculation of divertor impurity radiation usually requires a self-consistent calculation of plasma parameters, since diagnostic coverage is much less complete compared to the core plasma. For time-independent conditions, a 2-point model for a flux bundle which connects midplane and target can be used to obtain a reasonable description of plasma parameters with a self-consistent treatment of radiative losses [21] [22] [23] [24]. In the 2-point model, the heat flows parallel to the field line, where the electron pressure is conserved as long as momentum loss effects are omitted. The parallel thermal resistivity causes a temperature decay towards the target, while pressure conservation leads to a rise in electron density. The combined effect is a strong rise in local radiation densities towards the target plates.

The parallel heat flux is entrained in a toroidally symmetric plasma bundle which is fed by power leaving the plasma in the outer midplane. The thickness of the bundle is chosen to be equal to the power width λ_{int} in the outer midplane multiplied by a geometrical factor $sin(tan^{-1}(B_\theta/B_\phi)) \approx B_\theta/B_\phi \approx 0.3$ which takes into account the
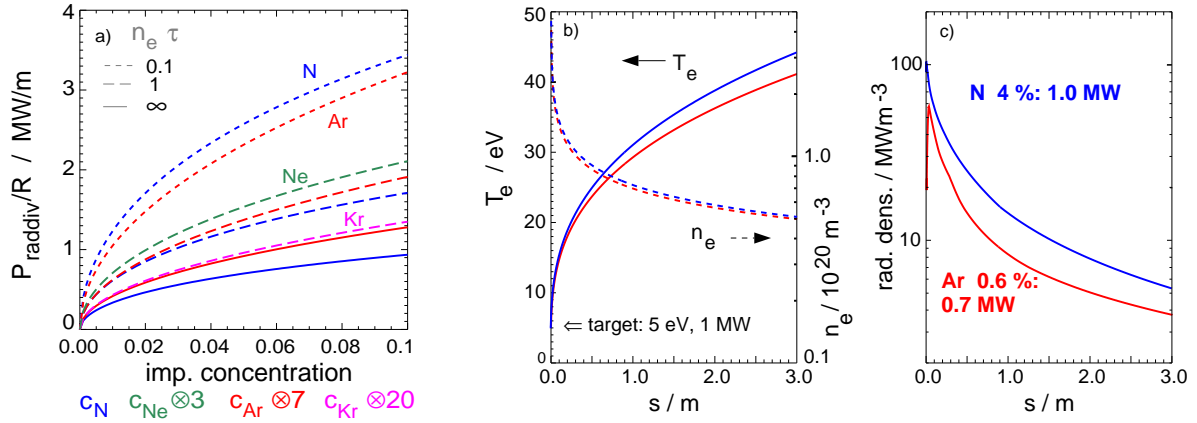
Figure 3. a) *Maximum normalized total divertor impurity radiated power P_{raddiv}^{max}/R according to equations 5 and 6 for different seed impurity species versus impurity concentration c_z. short dashed lines: non-equilibrium enhanced values $n_e\tau$= 0.1 ms 10^{20} m^{-3}, dashed lines: $n_e\tau$= 1 ms 10^{20} m^{-3} solid lines: coronal equilibrium values. AUG typical parameters were used: $n_{e,omp}$= 3 $\cdot10^{19}$ m^{-3}, $T_{e,omp}$= 80 eV, N_{div}=2, $A_\perp$= 0.014 m^2. b), c) Plasma profiles and radiation distribution along a flux tube starting from the outer target at s= 0 m (N_{div}=1). Shown are the first 3 m in the divertor, where most of the radiation is emitted. Indicated radiated powers were integrated from s= 0 ... 15 m, the connection length to the midplane. Experimental conditions were chosen similar to inter-ELM conditions of the discharge # 29254 shown in figures 4, 5. A divertor impurity enrichment by a factor 3 was assumed. The divertor n_e was set to match $n_{e,omp}$= 3 10^{19} m^{-3}, n_e τ= 0.1 10^{20} m^{-3}ms.*

compression of the parallel heat flux due to its deviation from being perpendicular to the mid-plane.

$$q_\parallel = P_{sep}/(2\pi R_{omp}\lambda_{int}sin(tan^{-1}(B_\theta/B_\phi))) \qquad (1)$$

The denominator is the area of the flux bundle in the plane perpendicular to $q_\parallel$, $A_\perp$. λ_{int} can be inferred from thermography measurements under attached conditions and is expected to be appropriate here since the radiating region is situated close to the target. A value of 5 mm is assumed in the following corresponding to typical AUG conditions [7], which corresponds to a power width along the target of about 20 mm. The heat flow causes a temperature drop along the flux bundle given by

$$q_\parallel = -\kappa_0 T_e^{5/2}\frac{\partial T_e}{\partial x} \approx -2390\frac{J}{s\,m\,eV^{7/2}}\cdot Z_{eff}^{-0.3}T_e^{5/2}\frac{\partial T_e}{\partial x} \qquad (2)$$

The term $Z_{eff}^{-0.3}$ approximates the reduction of the thermal conductivity with increasing Z_{eff}. Divergence of the parallel heat flux is caused by radiation

$$\frac{\partial q_\parallel}{\partial x} = -n_e^2 c_z L_z(T_e) \qquad (3)$$

The final ingredient of the simple 2-point model is the conservation of electron pressure along the flux tube

$$n_e(x)T_e(x) = const. = n_{e,omp}T_{e,omp} \qquad (4)$$

6

Momentum loss processes (charge-exchange, recombination) and ELMs are neglected which is probably the most severe deficiency of this model. Nevertheless, suitable dependencies on experimental parameters and comparisons of the effects of different impuritiy species are expected. An analytical solution of the equation set reveals the radiated power flux density [22]

$$
\begin{aligned}
q_{rad} &= (q_{omp}^2 - q_{tar}^2)^{0.5} \\
&= n_{e,omp} T_{e,omp} \left(2\kappa_0 c_z \int_{Te,tar}^{Te,omp} L_z(T_e) T_e^{0.5} \, Z_{eff}^{-0.3} \, dT_e\right)^{0.5} \ [W/m^2]
\end{aligned}
\tag{5}
$$

Numerical inspection shows that q_{rad} depends for realistic conditions only weakly on the temperature at the target $T_{e,tar}$ and is nearly proportional to the electron pressure in the outer midplane. The maximum radiated power density, q_{rad}^{max}, is obtained for vanishing target power flux density, $q_{tar}=0$. The maximum divertor radiated power is finally obtained by multiplication of q_{rad}^{max} with the perpendicular area and the number of divertors, $N_{div}= 2$.

$$
P_{raddiv}^{max} = q_{rad}^{max} A_\perp N_{div}
\tag{6}
$$

Figure 3a shows the normalized maximum divertor radiated powers calculated for different species according to equations 5 and 6 using the atomic data introduced in figure 1 for typical AUG conditions. The moderate saturation of the radiated power with increasing impurity concentration c_z is caused by a shrinking of the radiating zone due to the reduction of thermal conductivity. For constant impurity concentration, electron density, power width λ_{int} and geometry factor, P_{raddiv} is proportional to the circumference and thus the major radius R, suggesting P_{sep}/R as a similarity parameter for divertor radiation. The radiation levels obtained from eqs. 5 and 6 should be carefully considered since the boundary conditions (midplane T_e, target T_e) are just employed and not self-consistently calculated with the power flux. This can be done by solving the 2-point model, eq. 2-4 numerically. An example is shown in figures 3b,c, where experimental conditions for the outer divertor are used from AUG discharges introduced below. The analytical results from figure 3 are reconciled with 2-point modelling if the appropriate boundary conditions are assumed. The 2-point model allows the investigation of the effect of the connection length (and thus machine size) on $T_{e,omp}$ and thus, on P_{sep}/R. Only a moderate rise of the radiated power with connection length is obtained when the divertor density and temperature are kept constant, which is explained by the concentration of the radiation in the divertor region. The upstream $T_{e,omp}$ rises with connection length weakly $\approx s^{2/7}$. A reduced upstream $n_{e,omp}$ is therefore obtained for a larger device for identical divertor conditions due to the assumption of constant pressure along a field line. The simple model described above omits effects of target inclination and geometry on the divertor radiation, which are expected to enter via the spatial distribution of neutral recycling.

4. Radiative cooling experiments in the ASDEX Upgrade tokamak

Figure 4 shows time traces of 2 AUG discharges with nitrogen (feed-forward) and argon (feedback controlled via the measured power flux into the divertor) injection. After the impurity puff, the nitrogen case shows a predominant rise of divertor radiation, while with Ar only the main chamber radiation is enhanced. The initial rise of Z_{eff} is about 0.5 in both cases, at 3.5 s the N concentration from CXRS is about 1.3 %, the Ar concentration derived from SX spectroscopy is about 0.2 %. Spectroscopic measurements employing the NI line at 399.5 nm reveal a divertor enrichment c_{div}/c_{core} [25] of nitrogen by a factor 3, albeit with considerable uncertainty. c_{div} is here the ratio of the neutral impurity and deuterium fluxes at the target, c_{core} is the impurity concentration n_z/n_e. The neutral D pressure in the divertor is 2 Pa, corresponding to $1\ 10^{21}$ atoms/m^3. The measured total rise of nitrogen divertor radiation by ≈ 2.5 MW corresponds to the prediction of the 2-point model shown in in fig. 3 where highly non-equilibrium conditions are assumed. For the outer divertor 1 MW is predicted, 1.4 MW are calculated for inner divertor conditions, $T_e = 2$ eV and $P_{tar,in} = 0.2$ MW. There is no visible rise of divertor radiation in fig. 4b probably due to the reduction of P_{sep} by the Ar core radiation. Therefore, the model for Ar divertor radiation cannot be assessed. Both impurity injections lead to a considerable increase of the sputtered tungsten flux close to the strike point, despite a reduction in electron temperature and power flux. This is shown in figure 5. The W sputtering is almost completely caused by low-Z/seed impurities during ELMs. The core plasma tungsten concentration is about $5\ 10^{-5}$ before the impurity puff in both discharges and diminishes by a factor 2 after the start of the N puff and stays about constant with Ar. At the end of the nitrogen seeded discharge, the N puff is increased to obtain full detachment of the outer strike point. This causes a rise of core density and main chamber radiation.

The expected core radiation during impurity seeding is calculated for the discharges of figure 4 using measured plasma profiles and impurity densities. Figure 6 shows calculated radiated power densities in the main plasma for the N and Ar seeded cases, respectively. The radiation by tungsten is also shown. According to the atomic data, there is considerable core radiation due to argon, but not due to nitrogen. The inclusion of non-equilibrium effects predicts a considerable increase of the radiated power in the outer plasma region for both species. However, the ansatz for the non-equilibrium radiation calculation, namely the initial neutral state of the atom, is not as good an approximation in comparison to divertor conditions. A direct comparison of the predicted radiation profiles with bolometer tomography turned out to be extremely difficult. The reason is the limited spatial resolution of bolometry in the pedestal region, where very steep gradients are expected, and the presence and variation of radiating zones in the high field side X-point and divertor region. Tomographic reconstructions from foil bolometer measurements are shown in figure 6 before and during N seeding. The strong radiation inside the X-point is attributed to insufficient spatial resolution of bolometry.
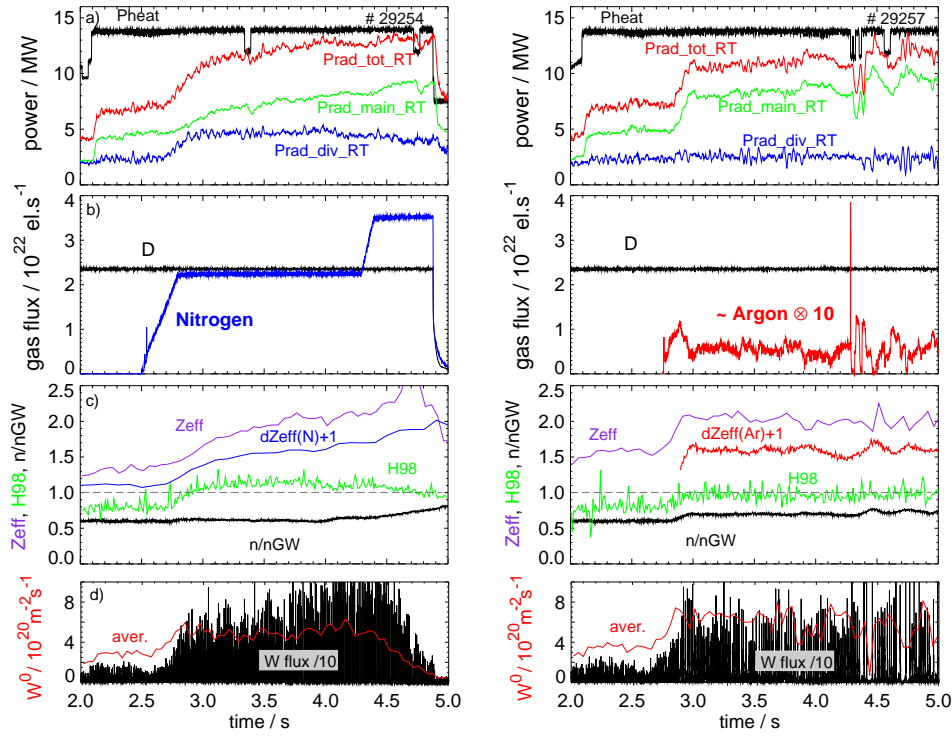
Figure 4. *Time traces of two discharges with nitrogen (left) and argon (right) seeding in otherwise identical conditions. a) heating power and radiated power from real time analysis [10]. b) puff rates. c) Z_{eff} from bremssstrahlung, contribution by N from CXRS, contrib. by Ar from soft-X spectroscopy. Spectroscopic measurements are evaluated (CXRS) or emissivity-weighted (SX-spectroscopy) around half-radius, bremsstrahlung tangency radius is $\rho_p=0.35$. d) neutral W influx close to the outer strike point.*

The nitrogen seeding causes a considerable energy confinement improvement, while the Ar injection a moderate one. The Ar injection causes a reduction of the ELM frequency from 120 to 70 Hz and also a slight rise of the electron density. With N, ELMs get shorter and slightly more frequent. The confinement improvement with nitrogen is clearly related to improved pedestal performance [28] [29]. TRANSP analysis reveals quite similar values of χ_i, χ_e in the core plasma. Figure 7 shows full profiles of electron temperature and density and pedestal profiles of the ion temperature and the radial electric field before and during the improved confinement phase with nitrogen injection. A deeper negative E_r well in the edge transport barrier and enhanced ion and electron temperatures are observed during the improved phase. The higher temperature persists over the whole plasma radius and causes the higher energy content. Ion dilution at constant pressure gradient would suggest about 15 % higher T_i values at the pedestal top. The observed effect is more pronounced, therefore non-linear effects have to be involved.

Recently, krypton has been added to the suite of AUG radiating species. It can be used alternatively to argon as a core radiator, with feedback gains [12] reduced by the
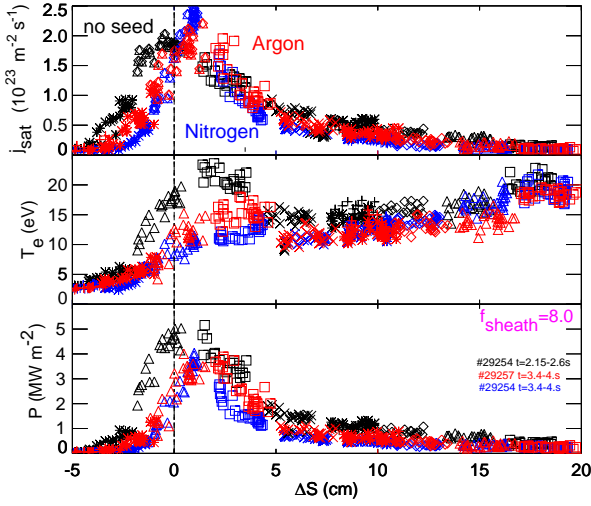
Figure 5. *Profiles of ion saturation current, electron temperature and heat flux from Langmuir probes for the discharges in figure 4, comparing the phases before impurity injection and during N and Ar seeding.*
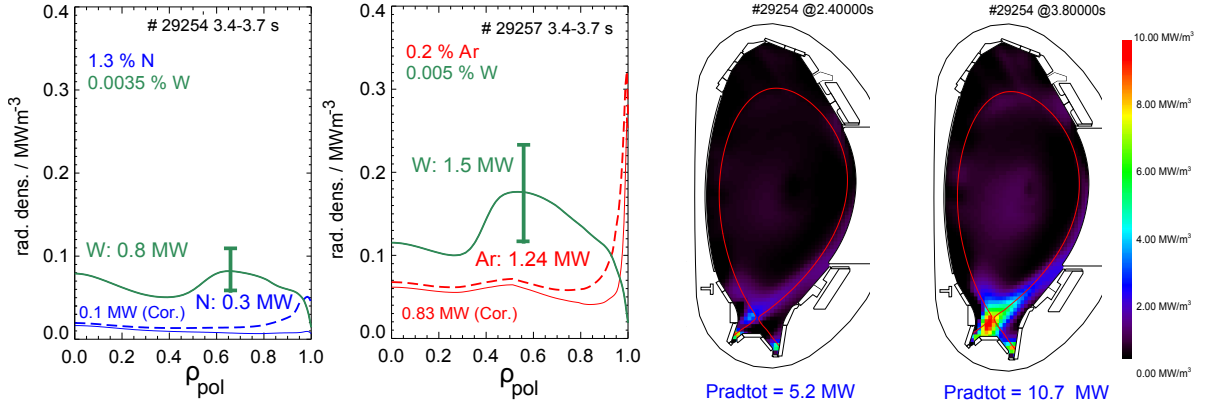

Figure 6. *left: Core profiles of the radiated power densities by N, Ar both under equilibrium and non-equilibrium conditions for the two discharges introduced in figure 4. The non-equilibrium parameter $n_e \tau$ has been calculated using the measured electron density and a simple estimate was made for the residence time τ: $\tau = 10$ ms outside $\rho_p = 0.95$, $\tau = 100$ ms at $\rho_p = 0$ with a quadratic decay to the value at $\rho_p = 0.95$ as expected from diffusion in a cylinder. W radiation in corona equilibrium has been calculated using the atomic data from [26]. right: deconvolution of foil bolometer measurements prior and during N seeding for # 29254.*

factor 0.3 to compensate the higher radiative capability of Kr. The advantage of Kr lies in the smaller fuel dilution for similar radiation levels in comparison to Ar. Figure 8a-c shows time traces of a high power discharge with combined N seeding for divertor control and Kr seeding for control of the power flux into the divertor. Radiation control is operational through the whole high power phase of the discharge, limiting the peak heat flux to acceptable values. With the last step in control of the power flux to the
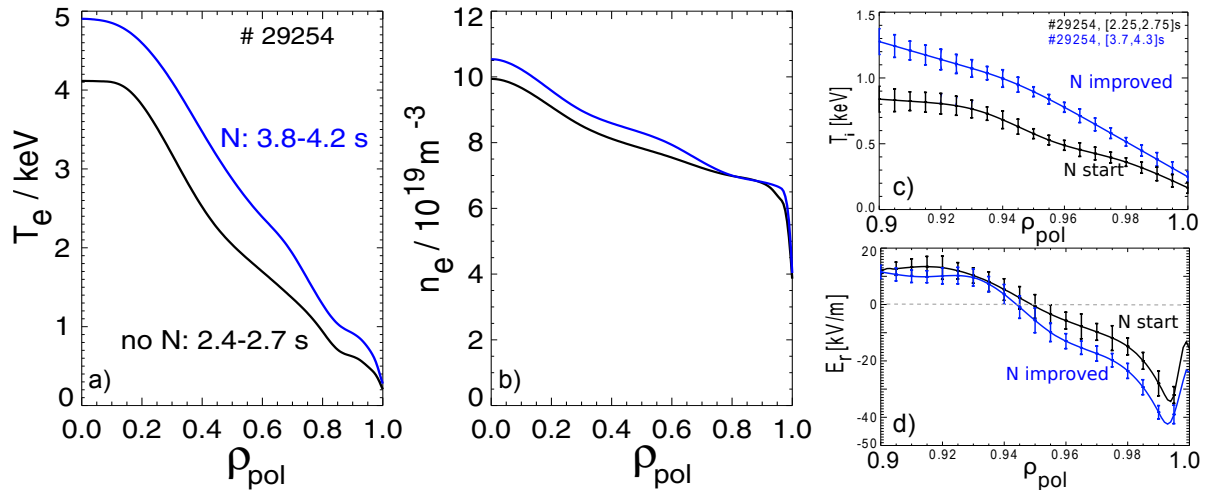
Figure 7. a) *Electron temperature profiles and b) electron density profiles from integrated data analysis using ECE, interferometry and Li-beam diagnostics for time intervals before and during N seeding. c) Pedestal profiles of ion temperature and d) radial electric field measured with CXRS [27] on nitrogen at the start of N injection and during the improved phase for the discharge shown in figure 4.*

divertor, partial detachment of the outer divertor occurs. Profiles of divertor plasma parameters for 3 distinct times are shown in figure 8d-f. The tomographic reconstruction for the highly radiating phase is shown in figure 8g, the total radiation is 18 MW and the Kr concentration derived from the core radiation is about 0.1 %. Figure 9 shows a discharge where the Kr radiation was enhanced up to the core radiation limit. Very good confinement, H_{98}=1.1, is obtained at high radiation level and $\beta_N \geq 3$ before a 4/3 NTM reduces the stored energy. Pronounced detachment with a peak power load below 1 MW/m^2 sets in at 4.6 s, resulting in an increase in line-averaged density from 1.25 to 1.45 10^{20} m^{-3} possibly by a change in the neutral fueling pattern. At t=5 s, central impurity accumulation sets in, presumably as a consequence of insufficient central heating. At 5.45 s, a locked mode is detected and the pulse is terminated by massive gas injection of neon. Attempts to stabilize the phase with pronounced detachment failed so far for plasma currents above 0.8 MA, but such pronounced detachment is not required for heat overload protection.

5. Divertor erosion

Apart from the limitation of the heat flux, the erosion of surface material has to be limited to ensure a sufficient lifetime of the plasma facing component. In the following, we assume tungsten as the plasma facing material, a maximum allowed erosion thickness of 5 mm and a required life time of 2 burn years (6.3 10^7 s) in a DEMO device. The allowed erosion thickness and lifetime correspond to 0.08 nm/s, or a maximum allowed net W erosion rate of 5 $10^{18} m^{-2} s^{-1}$ (W atomic density of 6.3 10^{28} W at/m^3). Due to a
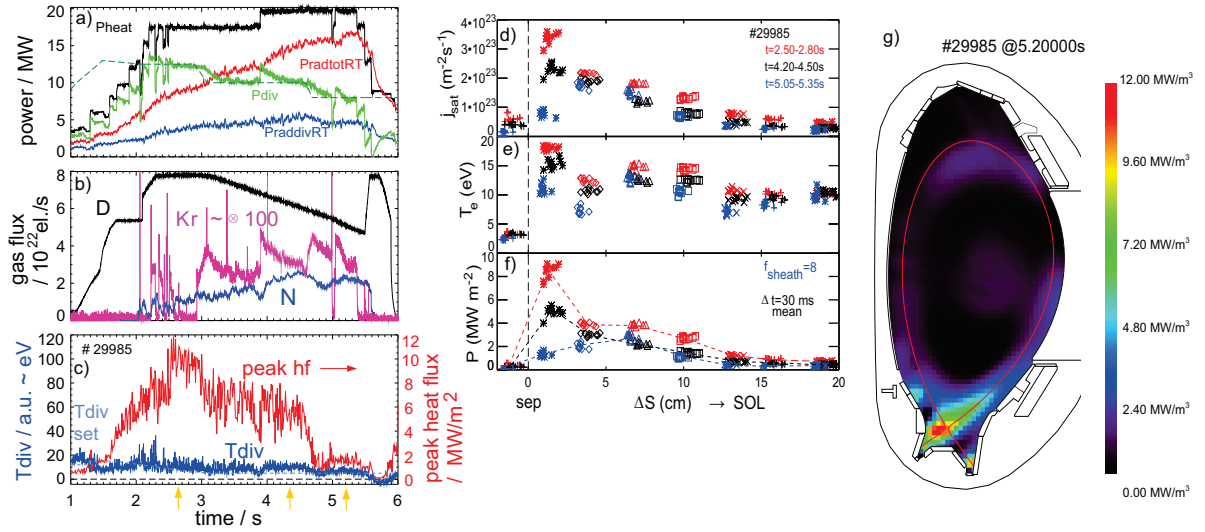
Figure 8. *Time traces for a discharge with combined N and Kr seeding for core radiation and divertor temperature/heat flux control. a) total heating power (NBI+ICRF+ECRH), total radiated power and divertor radiated power from simple real time algorithm, set value and actual value for power flux into divertor, $P_{div} = P_{heat}$-$P_{radmain}$. b) gas flux for D and N in el./s, approximate Kr flux (uncalibrated). c) set value and achieved value of Tdiv derived from thermocurrents [12] and time-averaged (ELMs) peak heat flux obtained from a Langmuir probe close to the strike point. d-f) Profiles of ion saturation current, electron temperature and power flux density along the outer target obtained from Langmuir probes. g) Tomographic reconstruction from foil bolometers for the partially detached divertor phase, $P_{rad,tot} = 18 \pm 1$ MW. $I_p = 1.2$ MA, $B_t = -2.5$ T, $q_{95} = 3.7$.*

considerable prompt redeposition fraction of the eroded W neutral flux, the permissible average peak erosion rate is increased. We assume a very conservative estimate of 80 % prompt redeposition [30], which results in a maximum W^0 flux of 2.5 $10^{19} m^{-2} s^{-1}$. Sputtering yields and rates for a typical divertor impurity composition under highly radiative conditions in AUG have been calculated using a Bohdansky formula and coefficients taken from [31]. As shown in figure 10, the divertor temperature in front of the target has to stay below 5 eV for the assumed impurity mix and a heat flux of 5 MW/m^2 for staying below the erosion limit. The measured fluxes and yields lie in the range expected from the sputtering yield. Typical inter-ELM W yields seen in figure 10 are a few 10^{-4} up to 10^{-3} for medium N seeding. The total W^0 influx is dominated by sputtering during ELMs, and the time-averaged W erosion is still about 10^{20} m^{-2} s^{-1}. It should be noted that the erosion during ELMs will be an over estimation since the prompt redeposition fraction will be higher during ELMs than the assumed 80 % due to a shortening of the W^0 ionization length. Nevertheless, ELM mitigation towards low peak ELM temperatures will be important to fulfill the erosion limit in DEMO, and dedicated calculations of the redeposition fraction as a function of plasma parameters will be required for optimization of divertor parameters regarding heat load and erosion
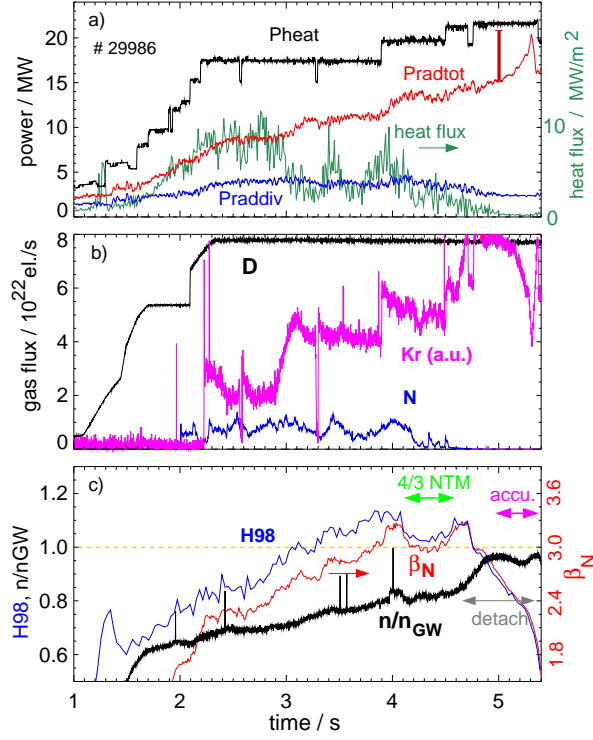
Figure 9. *Time traces for a discharge with combine N and Kr seding where the core radiation is brought to the limit by Kr injection. The real-time $P_{rad,main}$ shown is a lower limit, the error bar at t=5 s indicates the confidence interval of the total radiation from a tomographic analysis. I_p= 1.2 MA, B_t= -2.5 T, q_{95}= 3.7.*

limits.

6. Extrapolation to future devices

The recent finding about the size- and power-independence of the power width λ_q and analytic divertor radiation calculations suggest P_{sep}/R as the scaling parameter for the divertor radiation and heat load. λ_q was found to be inversely proportional to the poloidal magnetic field in the outer mid-plane. Some diffusive broadening of the heat flux channel towards the radiating zone close to the target is expected (parameter S in [5]), so finally a similar width of the heat carrying layer at the entrance of the highly radiating region is expected for AUG, ITER and DEMO. A value $P_{sep}/R \approx 15$ MW/m must be handled in ITER and DEMO without divertor overload and in DEMO, in addition, with low tungsten erosion. P_{sep}/R can be subdivided into components of divertor radiation by seed impurities and hydrogen, neutral fluxes from charge exchange and recombination and the heat flux accepted by the targets. A total divertor radiation $P_{raddiv}/R= 5$ MW/m has been achieved in AUG so far, in line with analytical predictions for highly non-equilibrium conditions and $n_{e,sep,omp}$= 5 10^{19} m^{-3}. The acceptable maximum target power flux is P_{tar}/R = 3-4 MW/m, depending on the heat flux imprint broadening by
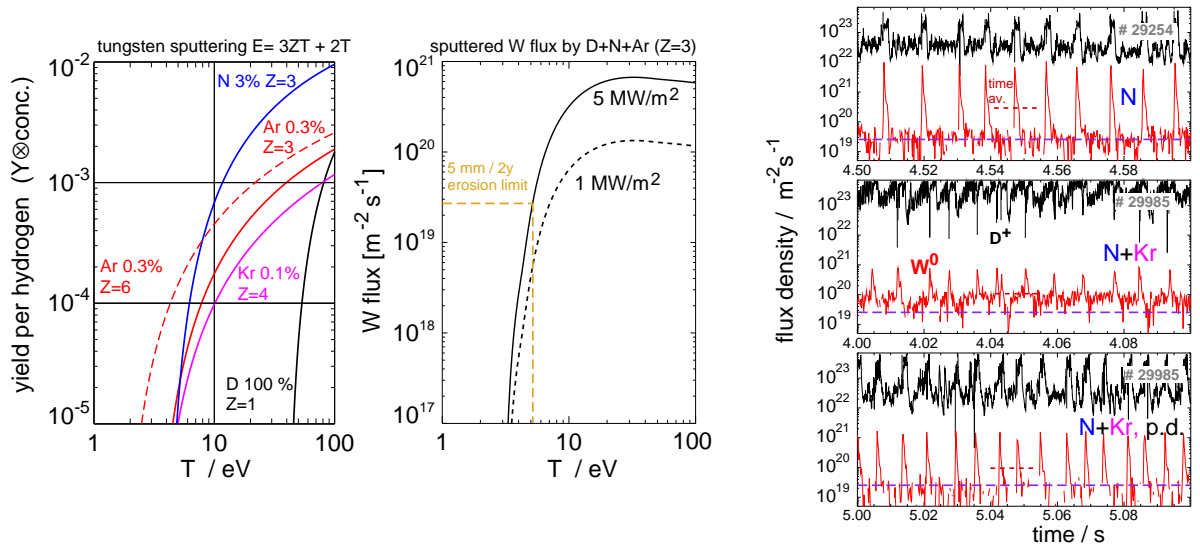
Figure 10. *left: Sputtering yields and sputtered fluxes of tungsten as a function of the temperature in front of the target, assuming $T_i=T_e$ and impact energy $E= 3ZT_e+2T_i$. Yields per impacting hydrogen ion (Y× concentration) for typical divertor compositions 3% nitrogen, 0.3 % argon at charge state Z=3, 0.1 % krypton at Z=4. For comparison also the D yield is shown and the argon yield for Z=6. mid: sputtered W flux by N + Ar (Z=3) + D vs. T assuming constant heat flux. The impacting D flux has been calculated from the heat flux assuming a sheath heat transmission factor of 7 and a recombination energy of 14 eV per e-i pair. right: measured ion flux from Langmuir probes and W^0 influx from spectroscopy a few cm above the strike point for discharges shown before with N and Kr seeding. The dashed lines indicate the time-averaged W flux (red) and its DEMO permissible time-averaged value (magenta).*

the partial detachment. Neutral power fluxes are not measured and cannot be easily quantified, assuming a CX flux comparable to the target ion flux $P_{CX}/R = 1$ MW/m appears as a very rough estimate. In order to reach the required value of P_{sep}/R, the divertor radiation must be increased. In AUG, this will be done by increasing the neutral divertor flux and hence the edge density, in line with ITER divertor modelling predictions [8]. This will first be conducted by a reduction of the pumping speed. Also an optimization of the vertical target divertor regarding recycling pattern and impurity enrichment may become possible in the future.

The core radiation for DEMO for given plasma parameters and impurity concentrations can be predicted using atomic data and specified plasma profiles. Figure 11 shows predicted radiation profiles in a DEMO plasma for Kr and Ar assuming concentrations required to achieve substantial core radiation levels above 300 MW. Also shown is the W radiation for an assumed concentration of $5\ 10^{-5}$. Non-equilibrium effects are not very important for DEMO parameters. With the AUG model scaled with $\tau \propto a^2$, an enhancement by 6 % is found for Kr and by 11% for Ar. A size scaling for core radiation with fixed density and impurity concentration from AUG to DEMO size has been produced by numerical integration comparing the computed impurity R_{AUG} to

$5 \times R_{AUG}$, and assuming $T_{DEMO}(\rho) = 5 \times T_{AUG}(\rho)$. The radiation rise with Ar under these assumptions is $\propto R^{2.2}$, with Kr $\propto R^2$. The weaker dependence compared to the strictly geometric $\propto R^3$ scaling results from the decrease of L_z with T and the reduction of non-equilibrium effects in the larger device. The stated size scaling has to be taken with care in particular due to the quite arbitrary profile scaling. Nevertheless, a more favourable extrapolation of core seed impurity radiation from small to large devices compared to divertor seed radiation can be concluded. The performance degradation by core radiation under reactor conditions is so far not known. First principle transport calculations are required which have to include the radiation losses.
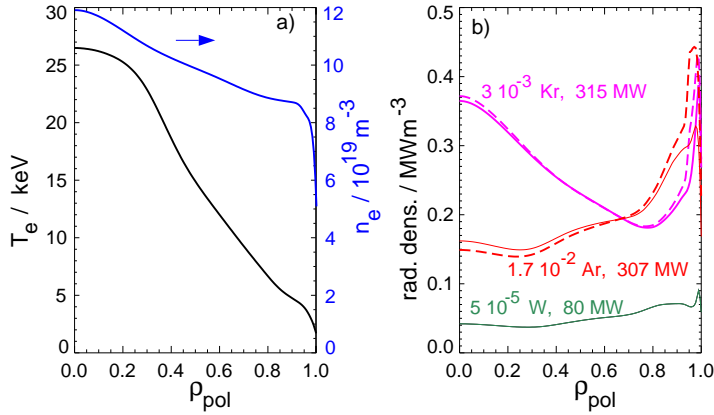

Figure 11. *a) assumed plasma profiles (scaled from an AUG Ar seeded plasma for a line-averaged density of 10^{20} m^{-3} and Te(0)=26.5 keV) and b) radiation profiles for Ar, Kr and W, with concentrations ($c_z(\rho= const.)$ and coronal radiated powers indicated. Dashed lines show non-equilibrium radiation densities. DEMO size parameters used are major radius R= 9 m and minor radius a=2.25 m.*

Figure 11 suggests that Ar is more suitable for DEMO compared to Kr due to its lower relative central radiation. However, the fuel dilution has to be considered as well. The average charge state at T_e= 15 keV is $\overline{Z}(Ar)$= 17.9 and $\overline{Z}(Kr)$= 34, resulting in substantial central Z_{eff} contributions of 5.1 by Ar and 3.4 by Kr for the concentrations indicated in figure 11. Fuel dilution is the more critical quantity, $n_{e,Ar}/n_e$= 0.3 and $n_{e,Kr}/n_e$= 0.1 are obtained for the assumed conditions. For reference, the average charge of W is 63.4 and the corresponding dilution is only 6.3 10^{-4}. The high dilution by Ar would reduce the fusion rate by a factor 2.

7. Conclusions

Possibilities and effects of the introduction of impurities for radiative plasma cooling in the core and divertor plasma have been assessed using simple analytical models and experimental observations, in view of the future requirements in ITER and DEMO. Strong core radiation will be required in DEMO to infer as small as possible divertor heat fluxes for coping with the relatively weak (compared to the heating power) power

handling capability of the divertor. Core radiative losses are induced by the injection of argon or krypton and can be predicted from specified plasma profiles and impurity concentrations. Here, a high electron density is the best means to achieve a high absolute radiation level and acceptable fuel dilution. In ITER, relatively low core radiation will be permitted due to the proximity of its operation to the L-H threshold. Both ITER and DEMO will require high divertor radiation to produce partial detachment for avoidance of divertor heat overload and excessive surface erosion rates. For semi-detached divertor conditions, the erosion is dominated by (already small) ELMs, and the maximum permissible ELM size may thus be even more constrained than by the heat-load restrictions.

The prediction of SOL and divertor radiation is less reliable compared to the core radiation due to uncertainties in plasma parameters and time-dependent effects on the radiation emission like the non-equilibrium radiation enhancement. Analysis of the simple 2-point model suggests that the quantity P_{sep}/R is an appropriate scaling parameter for divertor radiation and hence for acceptable divertor power fluxes. For equal upstream plasma densities, near-identical plasma conditions are expected for equal P_{sep}/R values in devices of different size. This scaling also shows that divertor power exhaust is more difficult in large devices since the power is expected to increase faster than $\propto R$. Core power exhaust appears easier in this respect, since the radiative losses scale more favourably, about $\propto R^{2-2.2}$ if the reduction of L_z with higher T and weaker non-equilibrium effects in the larger device are taken into account.

The consequences for the energy confinement are not yet clear, and this is an important topic for future studies. Nitrogen seeding has shown a positive effect on pedestal and hence global confinement in AUG in particular for high values of β_N and P_{sep}/P_{LH}. Krypton radiation allows good global confinement ($H_{98}= 1.1$) despite strong D puffing at very high heating powers and β_N values. Since central radiative losses are not expected to have a positive effect on confinement, the good performance is attributed to the indirect effect of the technical possibility to inject higher heating powers (and thus achieving a high β_N) without triggering a divertor load protection trip. It is clear that first principle modelling will be required for the prediction of energy confinement under radiative conditions in future devices.

High divertor radiation levels can be expected with nitrogen or argon seeding when a sufficiently high divertor compression/enrichment can be achieved. So far, argon injection in AUG causes predominantly main chamber radiation losses, and changes in the divertor radiation are attributed to a reduced power influx. The situation may change when a high enrichment of Ar in the divertor is achieved. The enrichment directly enters into the balance of core and divertor radiation, but its measurement bears substantial uncertainties. 2-D codes are in principle capable of predicting the enrichment, but there is no model validation available now, and neither is a reliable extrapolation to different divertor conditions. The momentum loss processes, which are in particular effective in the inner divertor and which have strong impact on the divertor radiation, are also not yet reproduced by 2-D codes [32]. For an accurate calculation of

SOL and divertor radiation, both time-dependent effects of (even small) ELMs as well as momentum loss processes and drifts need to be taken into account.

A factor of two enhancement of the currently achieved P_{sep}/R values with a closed vertical target divertor is required for ITER and DEMO. Foreseen measures are an increase of the divertor neutral pressure and geometric optimization of the poloidal recycling pattern towards higher divertor impurity enrichment and promotion of partial detachment.

8. References

[1] PACHER, G. et al., Nucl. Fusion **47** (2007) 469.
[2] TOBITA, K. et al., Nucl. Fusion **49** (2009) 075029.
[3] KALLENBACH, A. et al., Journal of Nuclear Materials **415** (2011) S19.
[4] ZOHM, H. et al., Nucl. Fusion **53** (2013) 073019.
[5] EICH, T. et al., Phys. Rev. Lett. **107** (2011) 215001.
[6] GOLDSTON, R., Nucl. Fusion **52** (2012) 013009.
[7] EICH, T. et al., Journal of Nuclear Materials **438 Supplement** (2013) S72.
[8] KUKUSHKIN, A. et al., J. Nucl. Mat. in press (2013), doi:10.1016/j.jnucmat.2013.01.105 .
[9] KALLENBACH, A. et al., Multi-machine comparisons of divertor heat flux mitigation by radiative cooling with nitrogen, in *Proc. of the 24rd IAEA Fusion Energy Conference, San Diego, USA*, volume IAEA-CN-197, pages ITR/P1–28, Vienna, 2012, IAEA.
[10] KALLENBACH, A. et al., Nuclear Fusion **52** (2012) 122003.
[11] DUMORTIER, P. et al., Plasma Physics and Controlled Fusion **44** (2002) 1845.
[12] KALLENBACH, A. et al., Plasma Physics and Controlled Fusion **52** (2010) 055002.
[13] REINKE, M. et al., J. Nucl. Mater. **415** (2011) S340.
[14] GIROUD, C. et al., Nucl. Fusion **52** (2012) 063022.
[15] BEURSKENS, M. et al., The effect of a metal wall on confinement in JET and ASDEX Upgrade, this conference, submitted to PPCF (2013) .
[16] ADAS, www.adas.ac.uk/manual.php .
[17] CAROLAN, P. and PIOTROWICZ, V., Plasma Physics **25** (1983) 1065.
[18] SAMM, U. et al., Journal of Nuclear Materials **176-177** (1990) 273.
[19] PETRIE, T. et al., Nucl. Fusion **48** (2008) 045010.
[20] DUX, R. et al., Nuclear Fusion **51** (2011) 053002.
[21] LACKNER, K. and SCHNEIDER, R., Fusion Eng. and Design **22** (1993) 107.
[22] POST, D. et al., Phys. Plasmas **2** (1995) 2328.
[23] STANGEBY, P., *The Plasma Boundary of Magnetic Fusion Devices*, Institute of Physics Publishing, Bristol and Philadelphia, 2000.
[24] STANGEBY, P. C. and LEONARD, A. W., Nucl. Fusion **51** (2011) 063001.
[25] PITCHER, C. et al., Phys. Plasmas **7** (2000) 1894.
[26] PÜTTERICH, T. et al., Nuclear Fusion **50** (2010) 025012 (9pp).
[27] VIEZZER, E. et al., Review of Scientific Instruments **83** (2012) 103501.
[28] SCHWEINZER, J. et al., Nuclear Fusion **51** (2011) 113003.
[29] TARDINI, G. et al., Plasma Physics and Controlled Fusion **55** (2013) 015010.
[30] DUX, R. et al., Journal of Nuclear Materials **390-391** (2009) 858.
[31] ECKSTEIN, W. et al., *Sputtering data*, Report IPP 9/82, IPP Garching, 1993.
[32] WISCHMEIER, M. et al., Journal of Nuclear Materials **415** (2011) S523.